journal

J. Am. Ceram. Soc., 88 [1] 184–190 (2005)
DOI: 10.1111/j.1551-2916.2004.00002.x

Electron Irradiation Induced Transformation of $(Pb_5Ca_5)(VO_4)_6F_2$ Apatite to $CaVO_3$ Perovskite

Z. L. Dong and T. J. White*,†

Centre for Advanced Research of Ecomaterials, Institute of Environmental Science and Engineering, Singapore 637723, Singapore

K. Sun, L. M. Wang,* and R. C. Ewing

Department of Nuclear Engineering and Radiological Sciences, University of Michigan, Ann Arbor, MI 48109-2104

Crystallochemical changes of $(Pb_5Ca_5)(VO_4)_6F_2$ apatite under electron irradiation were examined by transmission electron microscopy. The apatite, a synthetic analog of vanadinite, was moderately stable towards a less intense 300-keV LaB_6 source, while it changed rapidly in structure when exposed to the higher flux of a 200-keV field emission gun. The electron beam induced transformation of vanadinite proceeds sequentially by (i) migration and loss of fluorine, (ii) lead volatilization and conversion to 2–5-nm platelets of a glaserite-type structure, and (iii) the reduction of V^{5+} to V^{4+} with the removal of lead and calcium oxide that leads to single-crystal $CaVO_3$ perovskite as the ultimate product. The phase transformations are interpreted based on the crystallographic relations among the $CaVO_3$ perovskite, the $(Pb_5Ca_5)(VO_4)_6F_2$ apatite and the glaserite-type structures, and compositional changes under electron irradiation.

I. Introduction

Soil contaminants such as lead, arsenic, mercury, and cadmium that degrade groundwater quality are subsequently absorbed by plants and animals, and can promote a variety of acute and stochastic medical conditions. Metal mobilization is therefore a problem of long standing. Typically, the treatment of heavy metal bearing wastes are studied on a case-by-case basis, and many thermal, biological, and physical/chemical treatment technologies have been used to manage industrial wastes and contaminated sites containing pollutants at low levels. For highly concentrated toxic metals and radioactive isotopes crystallochemical immobilization is often considered the technology of choice. Numerous studies have demonstrated the effectiveness of fixing hazardous inorganic materials in durable ceramics that can sustain high loadings and density. However, the diversity of such ceramics and the complexity of their environmental reactivities require the systematic study of each stabilization system under development.

Apatite-based ceramics have been widely investigated as their capacity to incorporate toxic heavy metals is inherently high.[1,2] Apatites also have low dissolution rates that in favorable circumstances of reuse or disposal can meet stringent environmental regulations. In general, the group can be described as $[A(1)_2][A(2)_3](BO_4)_3X$ with complete or partial filling of the A-sites by Na, Mg, Ca, Sr, Ba, Pb, Cd, La, or Ce, the B-site by V, P, As, S, Si, Ge, Cr, or B and X commonly by a halide or hydroxyl ion.[3] Some minerals (e.g., belovite) retain Th and U and their disintegration products. Within the group, hydroxyapatite (HAp) is the most thoroughly studied, as it is the main inorganic component of bones and teeth and its potential to concentrate lead,[4–6] cadmium,[7–9] and radionuclides[10] is also well documented. It has also been found that HAp degrades rapidly when exposed to high-energy electrons during transmission electron microscopy (TEM) studies.[11–15] This may have implications for the stabilization of β-emitting nuclides such as Sr-90 (average emission energy 196 keV) or Cs-132 (157 keV).

This report extends an earlier investigation which noted that vanadinite was more resistant than its phosphate analog to electron irradiation,[16] although the dose dependence and ultimate transformation products were not determined. In the present study, crystallochemical damage of the vanadinite $(Pb_5Ca_5)(VO_4)_6F_2$ was studied by a 200 keV TEM with a field emission gun (FEG-TEM) and a 300-keV TEM with a lanthanum hexaboride (LaB_6-TEM) source with less intense electron flux. Using this approach, the dose dependence of electron irradiation on damage ingrowth could be investigated, and in the case of the LaB_6-TEM simultaneous collection of microchemical and crystallographic information was possible. Even though the rate of modification is quite different in these two experiments, the transformation mechanism and final product are identical.

II. Structure of Mixed Metal Apatites

The crystal structures of $[A(1)_2][A(2)_3](BO_4)_3X$ $P6_3/m$ apatites possess two distinct A-sites, A(1) and A(2). In mixed metal compounds, the A(2) interstice is the preferred location for relatively larger cations while smaller cations enter the A(1) position. However, such partitioning is observed only in natural specimens or materials that have been subjected to long heat treatment. The $(Pb_5Ca_5)(VO_4)_6F_2$ vanadinite in its equilibrated state has such a structure and its crystallographic data is given in Table I.[17] The dominant crystallographic features are isolated VO_4 tetrahedra that are corner-connected to $[Pb/Ca(1)]O_6$ metaprism columns aligned parallel to [001] to form one-dimensional tunnels in this direction (Fig. 1). The idealized $[Pb/Ca(2)]O_5F$ octahedra has its coordination sphere expanded to seven, and is the preferred location for Pb^{2+} leading to a partitioning coefficient (k_{Pb}) of 0.17 rather than 0.66, as implied by the compositional formula.‡ The A(2) tunnels are rich in lead, is mobile due to the larger anion-coordination sphere and proximity to F^-, and readily exchange with species of similar size in dilute salt solutions. The X sites are also the loci for the activation of electron beam damage.

Carol Jantzen—contributing editor

Manuscript No. 10637. Received October 29, 2003; approved February 19, 2004.
Supported through A*STAR Grant 012 105 0123.
*Member, American Ceramic Society.
†Author to whom correspondence should be addressed. e-mail: tjwhite@ntu.edu.sg

‡$k_{Pb}(A1/A2) = (2-2N(Ca1))/(3-3N(Ca2))$ where N(Ca1) and N(Ca2) are the occupancies of Ca on the A(1) and A(2) sites respectively.

Table I. Crystallographic Data for Vanadinite of Ideal Composition $[Pb_5Ca_5](VO_4)_6F_2$ and Cell Constants of $a = 10.0124(2)$ and $b = 7.1880(1)$ Å[17]

Site	Scattering factor	Wyckoff symbol	x	y	z	B (Å^2)	N
A(1)	Ca^{2+}	4f	1/3	2/3	0.0059(12)	1.4	0.83
	Pb^{2+}						0.17
A(2)	Ca^{2+}	6h	0.2426(2)	0.0036(3)	1/4	1.7	0.32
	Pb^{2+}						0.68
B	V^{5+}	6h	0.4093(6)	0.3805(6)	1/4	0.6	1
O(1)	O^{2-}	6h	0.3393(18)	0.5057(17)	1/4	1	1
O(2)	O^{2-}	6h	0.6074(20)	0.4807(17)	1/4	1	1
O(3)	O^{2-}	6h	0.3499(11)	0.2639(12)	0.0583(14)	1	1
X	F^-	2a	0	0	1/4	1	0.6

III. Experimental Methods

The $(Pb_5Ca_5)(VO_4)_6F_2$ vanadinite was synthesized by solid reaction.[17] CaO (obtained by decomposition of AR grade $CaCO_3$ at 900°C), PbO, V_2O_5, and CaF_2 powders were mixed in stoichiometric proportions (4:5:3:1 respectively) and held in an alumina boat while fired in air at 800°C for 10 h, followed by a further 7-week annealing at 800°C to equilibrate the lead/calcium partitioning over the A(1)/A(2) crystallographic sites. Specimens for electron microscopy were prepared thus: a small quantity of vanadinite powder was dispersed ultrasonically in ethanol and a drop of suspension then deposited onto a holey-carbon-coated copper-grid and allowed to air dry. High-resolution TEM (HRTEM) was carried out with a JEOL JEM2010F TEM (JEOL, Tokyo, Japan) operated at 200 kV with a field-emission (FEG) source. X-ray energy-dispersive spectroscopy (EDS) and HRTEM were also conducted using a JEOL JEM3010 TEM at an accelerating voltage of 300 keV with a lanthanum hexaboride (LaB_6) source, and fitted with a Si(Li) X-ray analyzer.

For both sets of experiments, a low-background double-tilt holder was used to align crystals in [0001], $[2\bar{1}\bar{1}0]$ or $[10\bar{1}0]$ orientations. During irradiation the electron beam was not completely focused, but expanded sufficiently to illuminate entirely the crystal under study. Only slight specimen drift was observed. The duration of the TEM-FEG experiments was less than 15 min, and it was difficult to obtain images that did not show damage ingrowth. For the TEM-LaB_6 studies experiments of several hours' duration were possible, with intervening collection of selected area electron diffraction (SAD) patterns and EDS. The electron flux for the TEM-FEG and TEM-LaB_6 experiments was estimated to be of the order of 10^7–10^9 and 10^5–10^6 A/cm^2 steradian, respectively.

Table II. Microscope Parameters

Parameter	200 keV FEG	300 keV LaB_6
C_s (mm)	1.2	1.4
C_c (mm)	1.6	1.2
Semi-convergence (mrad)	0.5	0.5
Energy spread (eV)	0.6	1.6
Flux (A · cm^{-2} · steradian^{-1})	10^7–10^9	10^5–10^6

FEG, field emission gun.

HRTEM images of the perfectly ordered vanadinite were simulated using the multislice approach[18] based on the structure of $(Pb_5Ca_5)(VO_4)_6F_2$ determined by an earlier X-ray diffraction (XRD) refinement (Table I). Experimental and instrumental parameters used in the simulations are summarized in Table II. A set of images simulated bracketing the experimental conditions used for imaging in the FEG-TEM are shown in Fig. 2. Before comparison with the multislice simulations, experimental images were processed using Fourier transform (FT) methods and constrained with planar space group symmetries to obtain reconstructed projected potential maps.[19–22] Single HRTEM images collected near Scherzer defocus could be analyzed in this manner; however, through-focal series could not be collected due to damage ingrowth.

IV. Results

(1) Stage I Tunnel Diffusion

At low electron doses in the TEM FEG vanadinite [0001] crystals remain intact, at least to the level interpretable in

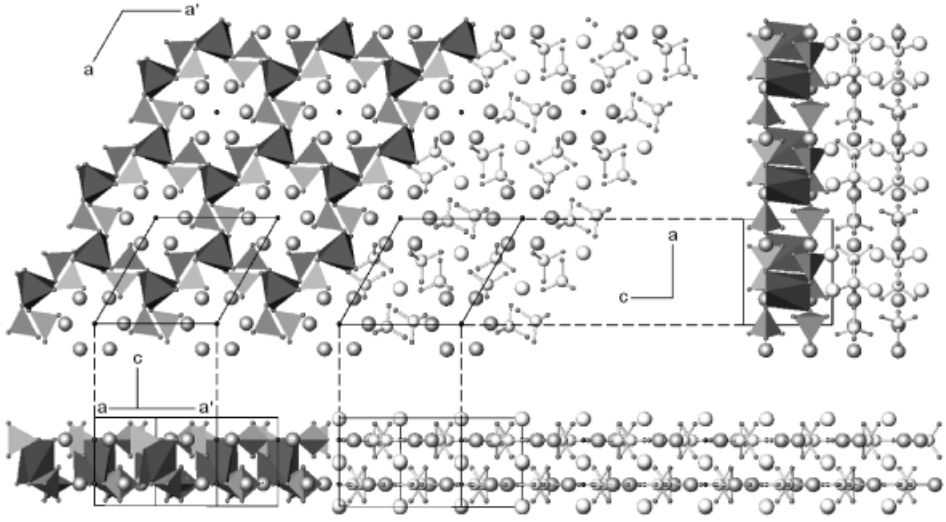

Fig. 1. $(Pb_5Ca_5)(VO_4)_6F_2$ vanadinite projected along its principal axes. Two representations are used. In one, the traditional emphasis on regular VO_4 tetrahedra in ball and stick format is given. In the other, the calcium-rich AO_6 metaprisms and VO_4 tetrahedra are highlighted to underscore the one dimensional tunnel structure. Ion exchangeable and electron-sensitive lead and fluorine are located in these channels.

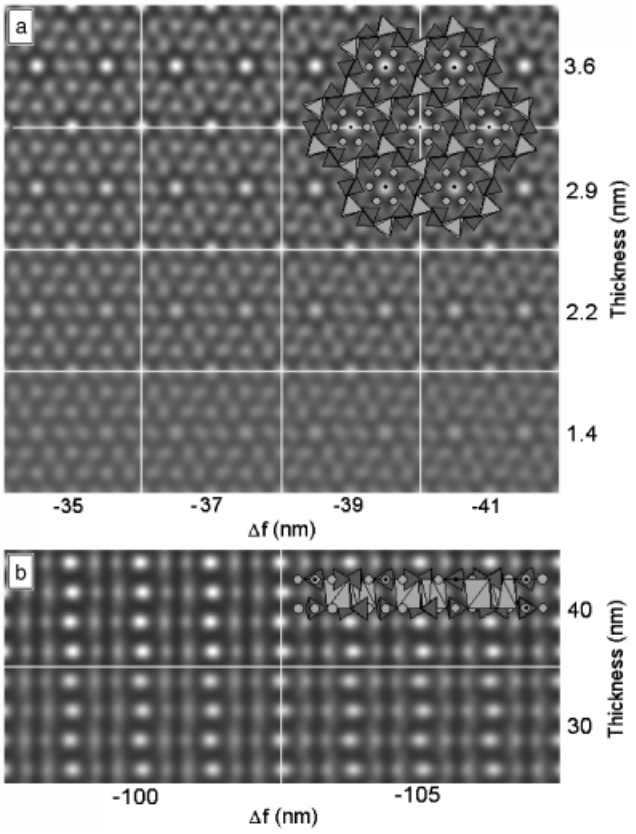

Fig. 2. Simulated HRTEM images of $(Pb_5Ca_5)(VO_4)_6F_2$ calculated for the (a) [0001] and (b) $[2\bar{1}\bar{1}0]$ zone axes. The conditions bracket those used for collection of experimental images in the FEG-TEM. The correspondence between the images and structure are shown in overlay.

high-resolution images. However, after an exposure of ≤ 1 min, damage became evident as mottled areas 2–3 nm in extent although the characteristic hexagonal array of bright dots (corresponding to the X anion columns) persisted (Fig. 3(a)). Fourier reconstruction of the images from such lightly damaged crystals yielded potential maps (Fig. 3(b)) readily constrained to p*6* symmetry (consistent with the [001] projection for $P6_3/m$) that were in good agreement with the simulated images (Fig. 2(a)). Similar concurrence was obtained for $[2\bar{1}\bar{1}0]$ projections where potential maps were constrained with the two-dimensional symmetry of p2gm ([100] for $P6_3/m$) (Figs. 2(b) and 3(d,e)).

(2) Stage II Cation Migration and Phase Separation

TEM-FEG irradiation for >1 min lead to decoration with disc-shaped (sometimes faceted) nanocrystals, inclusions, and etch pits with an average diameter of ~ 5 nm (Fig. 4). These were especially pronounced near the crystal edge and indicative of substantial lattice breakdown and migration of material. The hexagonal motif of white dots remained recognizable in thicker regions of the crystal wedge (Fig. 5 (a)), but reconstructed

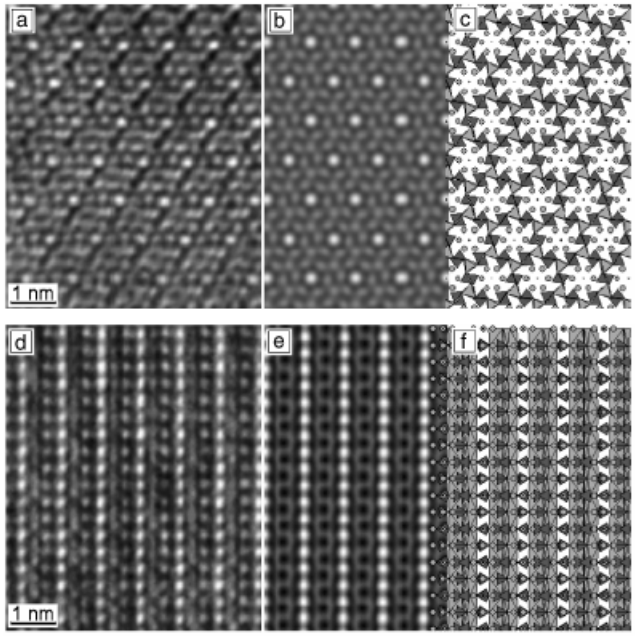

Fig. 3. High resolution images for vanadinate irradiated for <1 min in the FEG-TEM maintain the apatite structure. For the [0001] projection the (a) as-collected image; (b) processed image constrained by P*6* symmetry; (c) coincidence with the crystal structure projection are shown. The corresponding information for the $[2\bar{1}\bar{1}0]$ zone axis is presented in (d)–(f) with image processing constrained by p*2*gm symmetry.

images were incompatible with apatite, even with the imposition p*6* symmetry. However, the planar space group p*2*gm led to the reconstructed potential map shown in Fig. 5(b) that was consistent with image simulations modeled by a glaserite structure type (S.G. P-3*m*1) of nominal composition $(Ca,Pb,\square)_3V(VO_4)_2$ (Fig. 5(c)).

(3) Stage III Reduction and Recrystallization

Long-term irradiation carried out with the less intense LaB_6 TEM permitted tracking of structure evolution through collection of bright field images, diffraction patterns, and energy-dispersive X-ray analysis. During the first 10-min exposure, the surface of the particle was altered similarly to the 1-min FEG irradiation (Fig. 6(a,b)). With further exposure, the diffraction pattern contained additional Bragg reflections and diffuse intensity along $[\bar{3}210]^*$ indicative of the recrystallization of new phases (Fig. 6(b,c)). A weak diffraction ring indicates the formation of fine crystals and is consistent with the HRTEM images shown in Fig. 4. From 20 to 40 min the vanadinite diffraction pattern remains predominant although its relative intensity gradually diminishes. After 60-min exposure, vanadinite reflections continue to weaken, and new reflections consistent with $CaVO_3$ perovskite are recognizable (Fig. 6(d)). After 80 min, conversion to single-crystal perovskite is complete

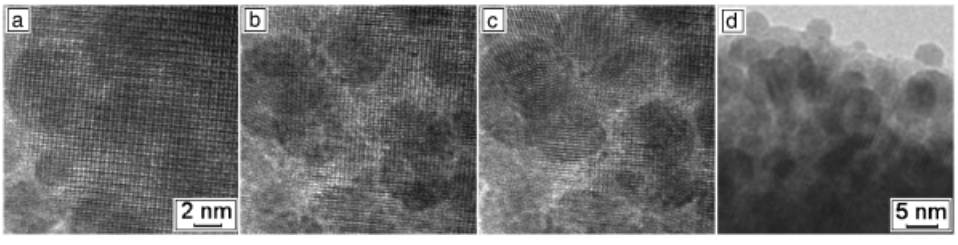

Fig. 4. The formation of calcium-rich glaserite-type 2–5-nm domains after irradiation for (a) less than 2 min, (b) 5 min and (c) 10 min. The parent apatite structure is oriented in $[2\bar{1}\bar{1}0]$. A lower magnification image (d) shows the migration of more volatile phases, presumed to be lead-rich glaserite and lead oxide, prior to vaporization.

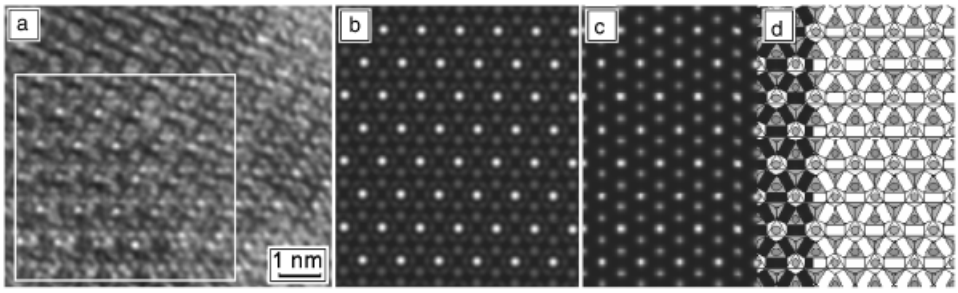

Fig. 5. A region of [0001] altered apatite containing a distinctive hexagonal array of bright spots. (a) Fourier processing of the region within the square using p*2*gm symmetry constraints yielded the highly symmetric image shown in (b). This image shows good agreement to a simulated image (c) calculated using Ca, Pb glaserite as the model. Correspondence between the image and the glaserite motif is emphasized in (d).

(Fig. 6(e)).[23] To maintain charge balance recrystallization was accompanied by the reduction of V^{5+} to V^{4+}. The removal of lead through volatilization (from the entire region under analysis) was quite small until the reaction was complete. Irradiation for a further 20 min resulted in no further changes. While the reaction sequence described above was most common, it was sometimes observed that V was driven out along with Pb before the complete perovskite recrystallization. In these cases CaO was the ultimate reaction product.

V. Discussion

(1) Relationship between Apatite, Glaserite, and Perovskite Structure Types

The transformation from apatite to perovskite is not unexpected crystallographically. The geometrical relationship between apatite and perovskite is most readily visualized and derived through a two-step change in the axes of reference illustrated in Fig. 6. If the unit cell vectors of the orthorhombic perovskite are

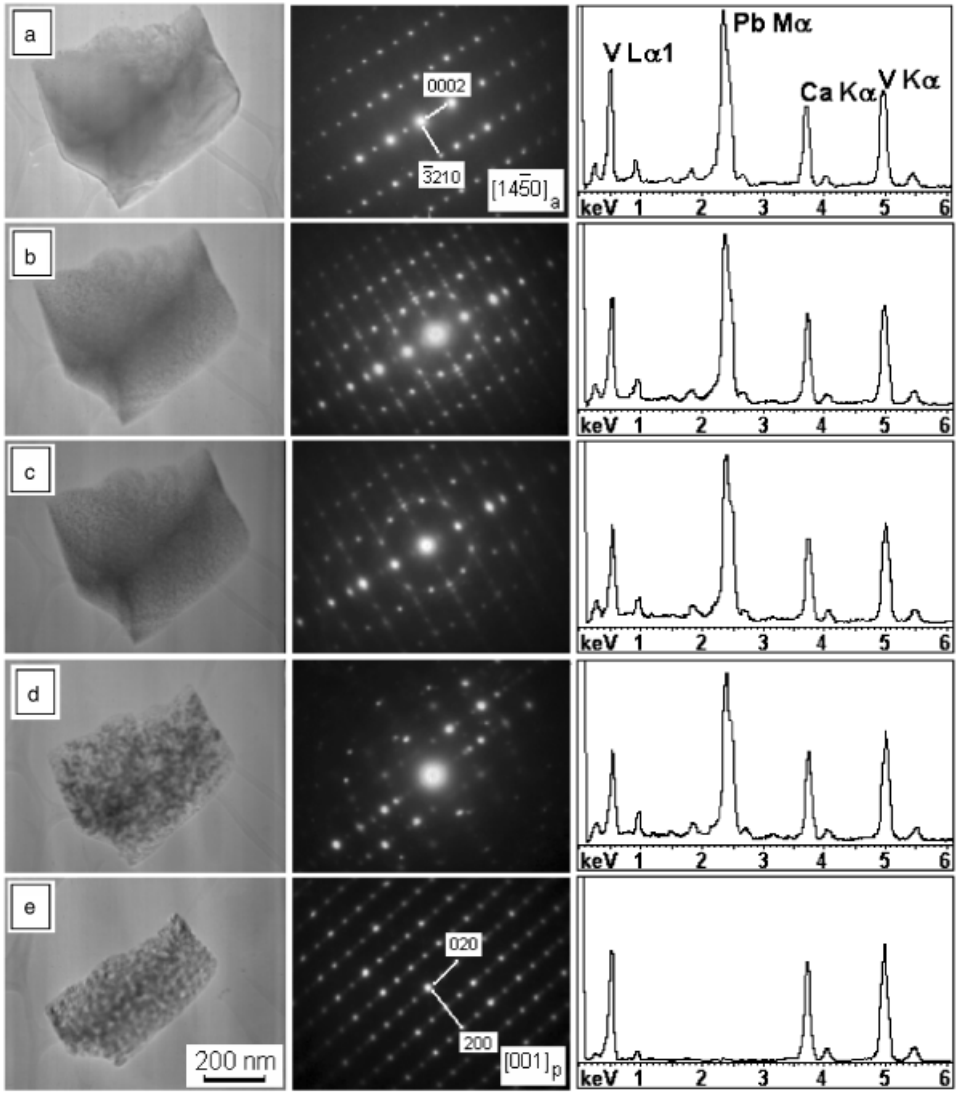

Fig. 6. Complete evolution of a $CaVO_3$ perovskite crystal from a $(Pb_5Ca_5)(VO_4)_6F_2$ apatite crystal during irradiation under LaB_6 emission as monitored by bright-field microscopy, electron diffraction, and energy-dispersive X-ray analysis. The cumulative irradiation times were (a) 0 min, (b) 10 min, (c) 20 min, (d) 60 min, and (e) 80 min. The external form of the apatite is preserved although there has been some crystal tilting during the experiment. Lead, calcium, and vanadium are slowly lost from the structure; however, the lead is not immediately transported away from the analysis region.

Table III. Comparison of Cell Constants Refined from X-ray Diffraction Data and Geometrically Transformed (A→P and P→A) Cell Constants Derived from These Values

Cell constants	Refined	Transformed	Comparison (%)
$(Ca_5Pb_5)(VO_4)6F_2$			
a (Å)	10.012	10.6612	+6.5
b (Å)	10.012	10.6792	+6.7
c (Å)	7.118	6.5185	−8.4
α (°)	90	90.0	0
β (°)	90	90.1	+0.1
γ (°)	120	120.1	+0.08
V_a (Å^3)	624.0	642.4	+2.9
c/a_{av}	0.71	0.61	−14
$CaVO_3$			
a (Å)	5.3171	5.5961	+5.2
b (Å)	7.5418	7.5085	−0.4
c (Å)	5.3396	5.0062	−6.2
α (°)	90	90.0	0
β (°)	90	90.0	0
γ (°)	90	98.6	+9.6
V_p (Å^3)	214.1	208.0	−2.8
V_a/V_p	2.9	3.1	6.9

The refined values for apatite and perovskite are taken from Dong and White[17] and Garcia-Jaca *et al.*,[23] respectively.

$\vec{a}_p, \vec{b}_p, \vec{c}_p$, the intermediate cell $\vec{a}_i, \vec{b}_i, \vec{c}_i$ and apatite are $\vec{a}_a, \vec{b}_a, \vec{c}_a$ then the transformation $\boldsymbol{T}_1$ is

$$\vec{a}_i = \vec{a}_p - \tfrac{1}{2}\vec{b}_p$$
$$\vec{b}_i = \vec{a}_p + \vec{b}_p$$
$$\vec{c}_i = \vec{c}_p$$

and $\boldsymbol{T}_2$ is

$$\vec{a}_a = \vec{b}_i - \vec{c}_i$$
$$\vec{b}_a = 2\vec{c}_i$$
$$\vec{c}_a = \vec{a}_i$$

The overall transformation from perovskite to apatite $\boldsymbol{T} = \boldsymbol{T}_2 \cdot \boldsymbol{T}_1$ can be expressed as

$$\begin{pmatrix} \vec{a}_a \\ \vec{b}_a \\ \vec{c}_a \end{pmatrix} = \begin{pmatrix} 1 & 1 & -1 \\ 0 & 0 & 2 \\ 1 & -\frac{1}{2} & 0 \end{pmatrix} \begin{pmatrix} \vec{a}_p \\ \vec{b}_p \\ \vec{c}_p \end{pmatrix}$$

and that for apatite to perovskite as

$$\begin{pmatrix} \vec{a}_p \\ \vec{b}_p \\ \vec{c}_p \end{pmatrix} = \begin{pmatrix} 1/3 & 1/6 & 2/3 \\ 2/3 & 1/3 & -2/3 \\ 0 & \frac{1}{2} & 0 \end{pmatrix} \begin{pmatrix} \vec{a}_a \\ \vec{b}_a \\ \vec{c}_a \end{pmatrix}$$

Ideally, the unit cell volume ratio of apatite:perovskite = 3:1. The geometrically derived cell constants are compared with those measured for $(Ca_5Pb_5)(VO_4)_6F_2$ (Table I) and $CaVO_3$ in Table III. It is remarkable that despite the apparent crystallographic dissimilarities of apatite and perovskite the divergence in unit cell volumes is only 2.9%. This small volume change explains why single-crystal integrity, as evidenced by the retention of shape in Fig. 6, is maintained despite substantial chemical dissociation.

The conversion of apatite to perovskite via glaserite is also possible crystallographically as illustrated in Fig. 8. As noted earlier, apatite is a one dimensional tunnel structure constructed of $A(1)O_6$ metaprisms that are corner-connected by BO_6 tetrahedra. The metaprism twist angle (φ) is flexible and highly sensitive to chemistry and crystal equilibration.[17] The X anion can be described as occupying a large octahedral "interstice" shown in Fig. 7(a). Apatite topology can be converted to that of glaserite by fixing $\varphi = 30^\circ$ to form more a regular octahedra (as viewed along [0001]) while at the same time rotating BO_4 tetahedra to align their threefold axes, rather than twofold axes, with the projected direction. In so doing, the large XO_6 octahedra are reduced to a size equivalent to the $A(1)O_6$ units (Fig. 7(b)). Perovskite can be derived from glaserite through reduction of vanadium and oxygen migration that converts isolated BO_4 tetrahedra to corner-connected BO_6 octahedra. At the same time larger A(2) cations migrate to fill the interstices created by topologically flexible $A(1)O_6$, BO_4 and BO_6 polyhedra. Increasing φ leads to compression of the metaprisms along $[0001]_a$, and consequently the discrepancy of the refined and transformed c_a parameter (−8.4%) is greater than for the a_a cell edge.

(2) Crystal Chemical Mechanism for Apatite to Perovskite Conversion

(A) Stage I Tunnel Diffusion: The X anions of apatite are mobile and readily exchanged for other anion or oxy-anion species. Their reactive and mobile nature in electron microscopy has been observed by many workers,[14,15] and in the case of hydroxyapatite $Ca_{10}(PO_4)_6(OH)_2$ complete conversion to $Ca_{10}(PO_4)_6O$ is possible.[24] It seems likely that incipient damage in vanadinite proceeds by a similar mechanism such that:

$$2F \rightarrow \square_F O^{2-} \quad (1)$$

$$(Ca_5Pb_5)(VO_4)_6F_2 \rightarrow (Ca_5Pb_5)(VO_4)_6O + F_2\uparrow \quad (2)$$

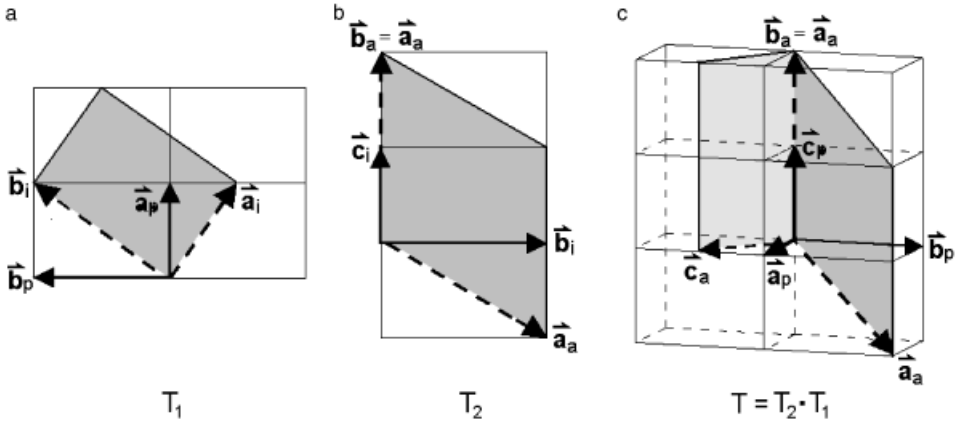

Fig. 7. The construction of lattice vectors for the conversion of (a) the orthorhombic cell of $CaVO_3$ perovskite ($\vec{a}_p, \vec{b}_p, \vec{c}_p$) via $\boldsymbol{T}_1$ to an intermediate phase ($\vec{a}_i, \vec{b}_i, \vec{c}_i$) and (b) the intermediate phase to apatite ($\vec{a}_a, \vec{b}_a, \vec{c}_a$) by $\boldsymbol{T}_2$. The overall change in cell axes is illustrated in (c).

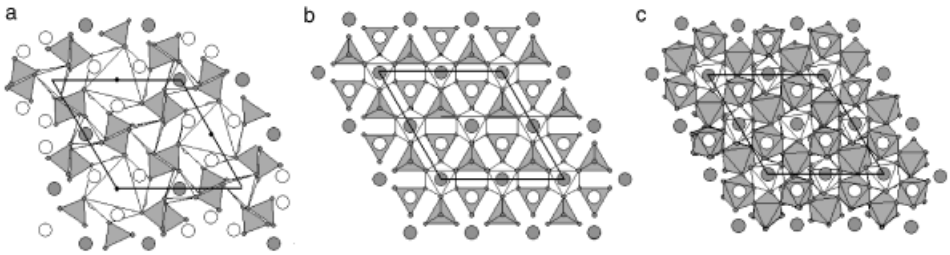

Fig. 8. The structural relationship between (a) [0001] $(Pb_5Ca_5)(VO_4)_6F_2$ apatite, (b) [0001] glaserite, and (c) [110] $CaVO_3$ perovskite. In (a) the large XO_6 octahedra are constructed to emphasize the topological relationship to glaserite. Through rotation the AO_6 metaprisms and XO_6 octahedra adopt a twist angle (φ) of 30° and the VO_4 tetrahedra align along their threefold axes. Finally, the V^{5+} is reduced to V^{4+} and the tetrahedra coalesce as corner-sharing octahedra. The real (non-idealized) structure of $CaVO_3$ is drawn.

For this replacement, the apatite framework remains intact, and as F/O weakly scatter electrons, high resolution TEM is relatively insensitive to such changes. Therefore, although subtle modification of the images was observed (Fig. 3) the overall structure is undifferentiated from apatite.[15]

(B) Stage II Cation Migration and Phase Separation: Subsequently, tunnel O^{2-} and Pb^{2+} are simultaneously driven from the apatite to yield $A_3(BO_4)_2$ structures of the glaserite type.

$$Pb^{2+} + O^{2-} \rightarrow \square_{Pb} + \square_{O} \tag{3}$$

$$(Ca_5Pb_5)(VO_4)_6O \rightarrow (Ca_5Pb_4)(VO_4)_6 + PbO\uparrow \tag{4}$$

At this point, dissociation and rearrangement of $A_3(BO_4)_2$ takes place to produce a volatile lead-rich glaserite that for a period adheres to the underlying crystal before being lost to the vacuum as recorded in Fig. 4(d).

$$(Ca_5Pb_4)(VO_4)_6 \rightarrow 2(Ca_{2.5}Pb_{0.5})(VO_4)_2 + Pb_3(VO_4)_2\uparrow \tag{5}$$

The higher melting point calcium-rich phase is more resistant to electron beam damage and less mobile, forming disk-like domains 20–50 nm in extent (Fig. 4(b,c)). A compositional continuum between the $(Ca_{2.5}Pb_{0.5})(VO_4)_2$ and $Pb_3(VO_4)_2$ glaserite probably exists. Moreover, several polytypes of the endmembers,[25–27] $Ca_3(VO_4)_2$, and $Pb_3(VO_4)_2$, can be created through the *c*-axis A-vacancy ordering, although it was not possible using the present data to differentiate which phase(s) dominate. The linear diffuse intensity in the diffraction patterns of Fig. 6(b,c) may be indicative of polytypic ordering. While the image analysis in Fig. 5 is consistent with glaserite crystallization, this projection would not reveal polytypic intergrowth, and over-interpretation should be avoided. Nonetheless, it is clear that vanadinite has been substantially altered to an intermediate compound(s).

(C) Stage III Reduction and Recrystallization: In the final stage, vanadium is reduced from pentavalent to tetravalent form.

$$2V^{5+} + O^{2-} \rightarrow 2V^{4+} + \square_{O} \tag{6}$$

During this process, the calcium-rich glaserite loses its remaining lead and some calcium to crystallize as perovskite.

$$2(Ca_{2.5}Pb_{0.5})(VO_4)_2 \rightarrow 4CaVO_3 + PbO\uparrow + CaO + O_2\uparrow \tag{7}$$

In this manner, apatite is converted through reconstructive transformation to single-crystal perovskite.

(3) Comparison of Phosphate and Vanadate Apatites

Although apatite crystal structures, particularly those of HAp, have been deeply studied using X-ray diffraction,[28–30] TEM has proved more difficult due to its instability under the electron beam that leads to monoclinic distortions and ultimately amorphization.[31,32] Aside from the formation of CaO no new phosphorous-bearing phases have been detected. This is in contrast to vanadinite where at least two new phases were identified directly—glaserite and perovskite types—and others are presumed to exist transiently (e.g., CaO, PbO). HAp is restricted in its transformation options because phosphorous must be pentavalent, differential volatilization (as occurred with Pb- and Ca-rich components of vanadinite) is impossible, and a "$CaPO_3$" perovskite entity cannot exist. Other apatites possibly susceptible to electron damage leading to recrystallization of new compounds, including perovskite or perovskite-related phases, include $Sr_5(VO_4)_3(Cu_{0.896}O_{0.95})$[33] to yield $SrVO_3$[34] and $Ba_5(MnO_4)_3Cl$[35] to yield $BaMnO_3$.[36] Recently, Boechat *et al.*[37] reported that reduction in hydrogen of $Ca_{10}(PO_4)_{6-x}(VO_4)_x(OH)_2$ with $x > 1.5$ also leads to the formation of $CaVO_3$, demonstrating the generality of the apatite–perovskite structural relationship for compounds containing multivalent tetrahedral species.

The underlying reasons for the higher stability of vanadinite compared with HAp have not been determined as this would require a computational approach used by Senger *et al.*[11] to estimate collision cross-sections for various ions. In this study, a relatively complex apatite was irradiated and it is unclear whether the $V \leftrightarrow P$ or $Ca \leftrightarrow Pb$ substitution were equally important in facilitating radiation resistance. Clarification of this point would require a comparative investigation of $Pb_5(PO_4)_3F$, $Ca_5(PO_4)_3F$, $Pb_5(VO_4)_3F$, and $Ca_5(VO_4)_3F$.

Acknowledgment

The authors would like to thank Ms. Wei Bing for her help in apatite powder sintering.

References

[1]Q. Y. Ma, S. J. Traina, T. J. Logan, and J. A. Ryan, "*In situ* Lead Immobilization by Apatite," *Environ. Sci. Technol.*, **27**, 1803–10 (1993).

[2]T. A. Ioannidis and A. I. Zouboulis, "Detoxification of a High Toxic Lead-Loaded Industrial Solid Waste by Stabilization Using Apatites," *J. Hazard. Mater.*, **B97**, 173–91 (2003).

[3]T. J. White and Z. L. Dong, "Structural Derivation and Crystal Chemistry of Apatites," *Acta Crystallogr.*, **B59**, 1–16 (2003).

[4]Y. Xu and F. W. Schwartz, "Lead Immobilization by Hydroxyapatite in Aqueous Solutions," *J. Contam. Hydrol.*, **15**, 187–206 (1994).

[5]E. Mavropoulos, A. M. Rossi, and A. M. Costa, "Studies on the Mechanisms of Lead Immobilization by Hydroxyapatite," *Environ. Sci. Technol.*, **36**, 1625–9 (2002).

[6]N. Arnich, M. C. Lanhers, F. Laurensot, R. Podor, A. Montiel, and D. Burnel, "*In Vitro* and *In Vivo* Studies of Lead Immobilization by Synthetic Hydroxyapatite," *Environ. Pollut.*, **124**, 139–149 (2003).

[7]Y. Xu, F. W. Schwartz, and S. J. Traina, "Sorption of Zn^{2+} and Cd^{2+} on Hydroxyapatite Surfaces," *Environ. Sci. Technol.*, **28**, 1472–80 (1994).

[8]J. Jeanjean, S. McGrellis, J. C. Rouchaud, M. Fedoroff, A. Rondeau, S. Perocheau, and A. Dubis, "A Crystallographic Study of the Sorption of Cadmium on Calcium Hydroxyapatite: Incidence of Cationic Vacancies," *J. Solid State Chem.*, **126**, 195–201 (1996).

[9]S. Mandjiny, K. A. Matis, A. I. Zouboulis, M. Fedoroff, J. Jeanjean, J. C. Rouchaud, N. Toulhoat, V. Petocek, C. Loos-Neskovic, P. Maireles-Torres, and D. Jones, "Calcium Hydroxyapatite: Evaluation of Sorption Properties for Cadmium Ions in Aqueous Solutions," *J. Mater. Sci.*, **33**, 5433–9 (1998).

[10]C. C. Fuller, J. R. Bargar, J. A. Davis, and M. J. Piana, "Mechanisms of Uranium Interactions with Hydroxyapatite: Implications for Groundwater Remediation," *Environ. Sci. Technol.*, **36** [2], 158–165 (2002).

[11]B. Senger, E. F. Bres, J. L. Hutchinson, J. -C. Voegel, and R. M. Frank, "Ballistic Damages Induced by Electrons in Hydroxyapatite (OHAP)," *Philos. Mag. A.*, **65** [3] 665–82 (1992).

[12]S. Nicolopoulos, J. M. Gonzalez-calbet, M. P. Alonso, M. T. Gutierrez-rios, M. I. de Frutos, and M. Vallet-Regi, "Characterization by TEM of Local Crystalline Changes During Irradiation Damage of Hydroxyapatite Compounds," *J. Solid State Chem.*, **116**, 265–74 (1995).

[13]K. Sato, T. Kogure, H. Iwai, and J. Tanaka, "Atomic Scale {10-10} Interfacial Structure in Hydroxyapatite Determined by High-Resolution Transmission El," *J. Am. Ceram. Soc.*, **85** [12] 3054–8 (2002).

[14]E. F. Brès, J. L. Hutchinson, B. Senger, J. -C. Voegel, and R. M. Frank, "HREM Study of Irradiation Damage in Human Dental," *Ultramicroscopy*, **35**, 305–32 (1991).

[15]F. J. G. Cuisinier, R. W. Glaisher, J. -C. Voegel, J. L. Hutchinson, E. F. Bres, and R. M. Frank, "Compositional Variation in Apatites with respect to Preferential Ionic Extraction," *Ultramicroscopy*, **36**, 297–305 (1991).

[16]Z. L. Dong, T. J. White, B. Wei, and K. Laursen, "Model Apatite Systems for the Stabilization of Toxic Metals: I Calcium Lead Vanadate," *J. Am. Ceram. Soc.*, **85** [10] 2515–22 (2002).

[17]Z. L. Dong and T. J. White, "Calcium Lead Fluoro-Vanadinites: I Disequilibrium Structure," *Acta Crystallogr.*, **B60**, 138–145 (2004).

[18]P. A. Stadelmann, "EMS – A Software Package for Electron Diffraction Analysis and HREM Image Simulation in Materials Science," *Ultramicroscopy*, **21** [2] 131–45 (1987).

[19]X. Zou, M. Sundberg, M. Larine, and S. Hovmoller, "Structure Projection Retrieval by Image Processing of HRTEM Images Taken under Non-Optimum Defocus Conditions," *Ultramicroscopy*, **62**, 103–21 (1996).

[20]D. N. Wang, S. Hovmoller, L. Kihlborg, and M. Sundberg, "Structure Determination and Correction for Distortion in HREM by Crystallographic Image Processing," *Ultramicroscopy*, **25**, 303–16 (1998).

[21]X. D. Zou, "Crystal Structure Determination by Crystallographic Image Processing: I.HREM Images, Structure Factors and Projected Potential"; pp. 163–72 in Materials Research Society Symposium Proceedings, *Electron Crystallography*, Edited by L. D. Douglas, S. Hovmoller, and X. Zou. Kluwer Academic Publishers, Dordrecht, 1998.

[22]X. D. Zou, "Crystal Structure Determination by Crystallographic Image Processing: II. Compensate for Defocus, Astigmatism and Crystal Tilt"; pp. 173–81 in Materials Research Society Symposium Proceedings, *Electron Crystallography*, Edited by L. D. Douglas, S. Hovmoller, and X. Zou. Kluwer Academic Publishers, Dordrecht, 1998.

[23]J. Garcia-Jaca, J. I. R. Larramendi, M. Insausti, M. I. Arriortua, and T. Rojo, "Synthesis, Crystal Structure and Transport Properties of a New Non-Stoichiometric $CaVO_3$ d phase," *J. Mater. Chem.*, **5**, 1995–9 (1995).

[24]P. A. Henning, A. R. Landa-Canovas, A. -K. Larsson, and S. Lidin, "Elucidation of the Crystal Structure of Oxyapatite by High-Resolution Electron Microscopy," *Acta Crystallogr. B*, **55**, 170–6 (1999).

[25]R. Gopal and C. Calvo, "The Structure of $Ca_3(VO_4)_2$," *Z. Kristallogr. Kristallg. Kristallphy. Kristallchem.*, **137**, 67–85 (1973).

[26]A. Grzechnik, "Crystal structure of $Ca_3(VO_4)_2$ synthesized at 11 GPa and 1373 K," *Solid State Sci*, **4**, 523–7 (2002).

[27]J. -M. Kiat, P. Garnier, and M. Pinot, "Neutron and X-ray Rietveld Analysis of the Three Phases of Lead Orthovanadate $Pb_3V_2O_8$: Importance of the Electronic Lone Pairs in the Martensitic Transitions," *J. Solid State Chem.*, **91**, 339–49 (1991).

[28]R. M. Wilson, J. C. Elliott, and S. E. P. Dowker, "Rietveld Refinement of the Crystallographic Structure of Human Dental Enamel Apatites," *Am. Mineral.*, **84**, 1406–14 (1999).

[29]A. Nounah, J. L. Lacout, and J. -M. Savariault, "Localization of Cadmium in Cadmium-Containing Hydroxy- and Fluorapatites," *J. Alloys Compds.*, **188**, 141–6 (1992).

[30]K. Sudarsanan and R. A. Young, "Structural Interactions of F, Cl and OH in Apatites," *Acta Crystallogr. B.*, **34**, 1401–7 (1978).

[31]M. Cameron, L. M. Wang, K. D. Crowley, and R. C. Ewing, "HRTEM Observation on Electron Irradiation Damage in F-Apatite," pp. 378–9 in Proceedings of the 50th Annual Meeting on the Electron Microscopy Society of America, Edited by G. W. Bailey and S. A. Small, San Francisco Press, San Francisco, CA, 1992.

[32]L. M. Wang, S. X. Wang, R. C. Ewing, A. Meldrum, R. C. Birtcher, P. Newcomer, W. J. Weber, and Hj. Matzke, "Irradiation-Induced Nanostructures," *Mater. Sci. Eng. A*, **286**, 72–80 (2000).

[33]W. Carrillo-Cabrera and H. G. von Schnering, "Pentastrontium Tris(tetraoxovanadate(V)) catena-monoxocuprate(I), $Sr_5(O_4)_3(CuO)$—An Apatite Derivative with Inserted Linear $(CuO)^{1-}$ Chains," *Z. Anorgan. Allgem. Chem.*, **625**, 183–5 (1999).

[34]J. Garcia-Jaca, J. L. Mesa, M. Insausti, J. I. R. Larramendi, M. I. Arriortua, and T. Rojo, "Synthesis, Crystal Structure, Stoichiometry and Magnetic Properties of $(Ca_{1-x}Sr_x)VO_3$," *Mater. Res. Bull.*, **34**, 289–301 (1999).

[35]D. Reinen, H. Lachwa, and R. Allmann, "EPR und Ligandenfeldspektroskopische Untersuchungen an Mn(V)-haltigen Apatiten sowie die Struktur von $Ba_5(Mn\ O_4)_3Cl$," *Z. Anorg. Allgem. Chem.*, **542**, 71–88 (1986).

[36]A. N. Christensen and G. Ollivier, "Hydrothermal and High-Pressure Preparation of Some $BaMnO_3$ Modifications and Low-Temperature Magnetic Properties of $BaMnO_3$ (2H)," *J. Solid State Chem.*, **4**, 131–7 (1972).

[37]C. B. Boechat, J. Terra, J. -G. Eon, D. E. Ellis, and A. M. Rossi, "Reduction by Hydrogen of Vanadium in Vanadate Apatite Solid Solutions," *Phys. Chem. Chem. Phys.*, **5**, 4290–8 (2003). □